Shear horizontal mode surface acoustic wave resonator with ultra-high electromechanical coupling based on the X-cut LNOI acoustic platform

Tiancheng Luo[1,*], Qibin Zeng[1], Weifan Cai[1], Zhi Shiuh Lim[1], Shengwei Zeng[1], Samantha Faye Duran Solco[1], Zhen Ye[1,2], Chee Kiang Ivan Tan[1], Seeram Ramakrishna[2], Huajun Liu[1,*]

[*]Authors to whom correspondence should be addressed: luo_tiancheng@imre.a-star.edu.sg; liu_huajun@ a-star.edu.sg

AFFILIATIONS

[1]Institute of Materials Research and Engineering (IMRE), Agency for Science, Technology and Research (A*STAR), 2 Fusionopolis Way, Innovis #08-03, Singapore 138634, Republic of Singapore

[2]Department of Mechanical Engineering, National University of Singapore (NUS), 9 Engineering Drive 1, Singapore 117575, Republic of Singapore

ABSTRACT

Shear horizontal surface acoustic wave resonators (SH-SAWRs) based on lithium niobate thin films on insulator (LNOI) platforms exhibit high electromechanical coupling and hold significant potential for applications in devices operating at frequencies exceeding gigahertz (GHz). This work presents the SH-SAWR with a resonance frequency of 2 GHz and high effective electromechanical coupling coefficient (k_{eff}^2) of up to 42%. Finite element analysis (FEA) and theoretical studies were combined to optimize the structural parameters of the device for higher k_{eff}^2 and larger quality (*Q*) factor, with the measured results effectively validating the proposed designs. Compared to devices without grating reflectors (GRs), the *Q* factor can be increased by over twofold with floating GRs and by threefold with grounded GRs. Our results show the outstanding performance of SAW resonators based on LNOI, promising for ultrawideband wireless communications.

I. INTRODUCTION

The development of radio frequency (RF) filters[1-3] has been a pivotal driver of advancements in wireless communication technology while microelectromechanical systems (MEMS) technology[4-6] is widely adopted, particularly in mobile terminals like smartphones, due to advantages in miniaturization and power consumption.

As core components in the RF filters, acoustic resonators play key roles in determining the operating frequency and bandwidth. Among different kinds of resonators, surface acoustic wave resonators (SAWR)[7-10] and film bulk acoustic wave resonators (FBAR)[11,12] have been the dominant technologies in the industry over the past three decades. SAWR exhibits notable advantages, including a relatively simple fabrication process, technological maturity, and low cost[9,13]. However, traditional SAWR devices are limited by their low resonance frequency (f_r) and small effective electromechanical coupling coefficient (k_{eff}^2). Consequently, SAWRs excel in low-to-mid-frequency applications but show weak competitiveness in high-frequency applications[14,15].

Smart-cut technology[16,17] has expanded the application of lithium niobate (LN) and lithium tantalate (LT) from bulk materials to thin films, revolutionizing LN and LT-based optical and acoustic devices. This progress has facilitated innovations like laterally excited bulk acoustic wave resonator (XBAR)[18-20] and thin-film SAWR. Compared to conventional SAWR based on bulk materials, thin-film SAWR can achieve higher quality (Q) factors and larger electromechanical coupling coefficients[21]. Additionally, the bonding SiO_2 layer used in the transfer process helps improve the frequency-temperature stability of these devices[22,23]. It is worth noting that among various LN and LT thin films, the fundamental horizontal shear (SH_0) mode SAWR based on X-cut LN exhibits significant performance advantages. By optimizing the electrode material and structural parameters, the device can be tailored to meet different application requirements. For example, SH-SAWRs with Au electrodes can not only achieve high Q values above 1 GHz but can also attain an k_{eff}^2 exceeding 40% through structural optimization[24,25]. Additionally, SH-SAWRs with lower-density Al electrodes can achieve f_r exceeding 10 GHz[26].

In this work, we present a SH_0 mode SAWR with a 1.97 GHz resonance frequency (f_r) and 42% effective electromechanical coupling coefficient (k_{eff}^2) based on the X-cut lithium niobate on insulator (LNOI) platform. Pt is employed here to provide another approach to achieve high k_{eff}^2 above GHz. Besides, grating reflectors (GRs) are optimized to improve device Q factors to more than three times. The finite element analysis (FEA)[27,28] is used to optimize the device design. The device fabrications were performed by E-beam lithography (EBL), E-beam evaporator, and lift-off processes [29-31]. The devices were measured by a customized RF probe station and a vector network analyzer (Rohde & Schwarz).

II. DESIGN AND MODELING

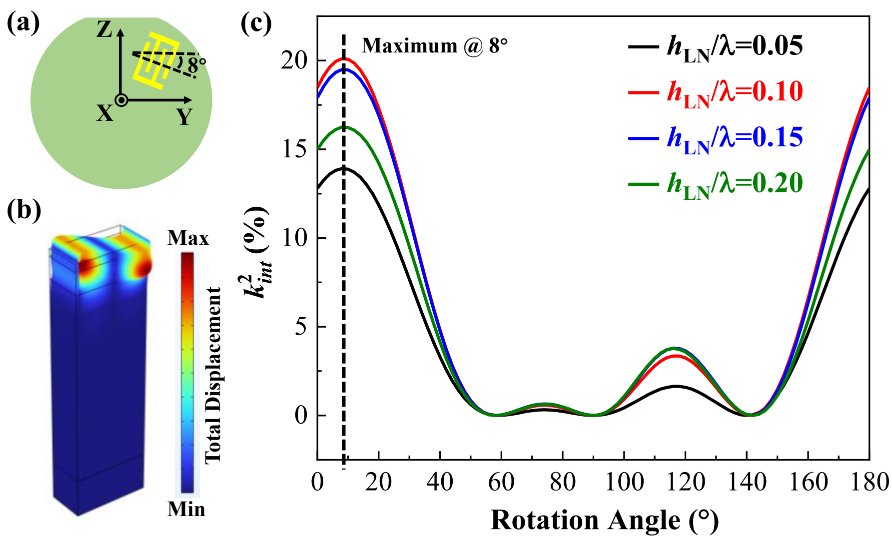

Figure 1. (a) Schematic of IDT rotation in YZ plane. (b) SH_0 mode shape and vibration displacement. (c) Simulated k_{int}^2 based on X-cut LN/SiO_2/Si substrate with different in-plane orientations.

To explore the maximum potential of the SH_0-SAWR, this work systematically investigated the effect of the interdigital transducer (IDT) rotation angle in the YZ plane on the intrinsic electromechanical coupling (k_{int}^2) of SH_0 mode which is calculated by eigenfrequencies of the model[32-34]. As shown in Figure 1, various wavelengths (λ) are also studied and the thickness of the LN and SiO_2 layer is set to 0.7 and 2 μm, respectively, due to the wafer availability. Besides, the simulation step is set to 2 degrees to find the orientation with the largest electromechanical coupling. Benefitted from the strong in-plane anisotropy of X-cut LN, the k_{int}^2 can be tuned from 0 to 20% by altering in-plane orientation while the maximum corresponds to 8°-rotation.

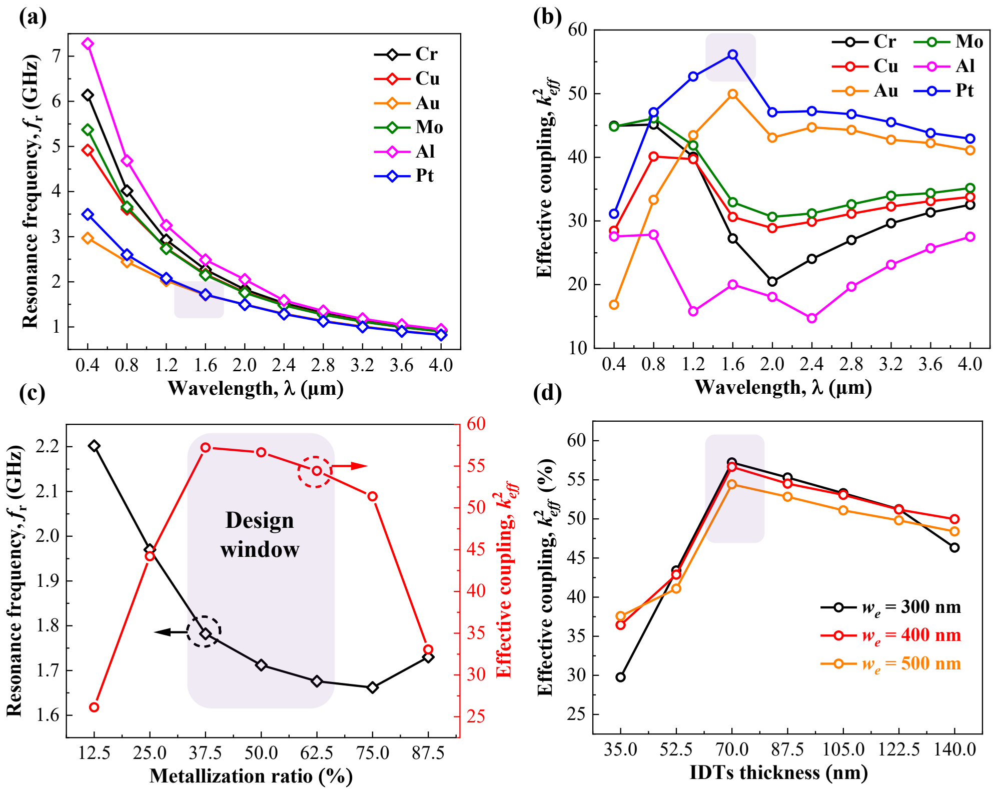

Figure 2. Effects of IDT material and λ on (a) f_r and (b) k_{eff}^2 of SH_0 mode. (c) Influence of metallization ratio on f_r and k_{eff}^2 when IDT material and λ are set to Pt and 1.6μm, respectively. (d) Variation of k_{eff}^2 with IDT thickness.

In addition to the IDT rotation, there are still many device design variables that will affect the device SH_0 mode electromechanical coupling, which are detailedly analyzed in Figure 2. Here, simulation in the frequency domain is employed and k_{eff}^2 is calculated to obtain a more direct estimation of the device electromechanical coupling capability. Figures 2(a) and 2(b) show the effects of IDT material and λ on f_r and k_{eff}^2 . According to the results, these six metals investigated can be clearly categorized into three groups. The first group includes Pt and Au, both of which enable higher k_{eff}^2 . Notably, the maximum k_{eff}^2 is obtained when Pt is adopted and the λ is set to 1.6 μm. However, for applications with stringent impedance requirements, Au offers a promising alternative due to its superior electrical conductivity. The second group consists of Cu and Mo. Compared to Pt and Au, SAWRs using Cu and Mo exhibit higher f_r, though typically at the cost of reduced k_{eff}^2 across most λ settings. While the k_{eff}^2 of Cu is slightly lower than that of Mo, Cu's significantly higher conductivity makes it a favorable choice for applications requiring moderate f_r and k_{eff}^2 . The third group includes Al and Cr. Among all materials, Al exhibits the highest f_r but the lowest k_{eff}^2 , whereas Cr provides the second highest f_r and the second lowest k_{eff}^2 across most λ settings. Considering both f_r and conductivity, Al emerges as the more suitable option in this group. In this work, the design goal is to maximize k_{eff}^2 . Therefore, Pt electrode with a 1.6 μm wavelength is adopted.

Furthermore, Figure 2(c) shows the effect of metallization ratio when the optimized IDT material and λ are adopted. SAWRs with metallization ratio between 37.5% and 62.5% shows a large k_{eff}^2 . Taking fabrication deviation into account, we set the metallization rate at the center of the design window, which is 50%. The final optimization is the IDT thickness. As shown in Figure 2(d), the maximum k_{eff}^2 occurs when the electrode thickness is 70 nm, which applies across different IDT widths (w_e).

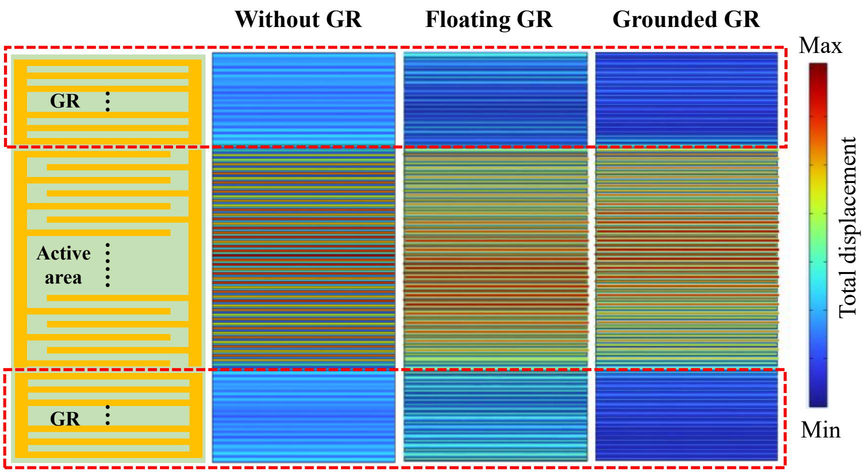

Figure 3. The FEA simulation of the resonance displacement and energy limitation of three different GR configurations: without GR (open), floating GR, and grounded GR.

Floating GRs are widely used in SAWRs to improve the Q factor[13,35,36]. The grounded GR structure is adopted here and they show a better improvement in Q factor. Figure 3 shows the simulated results of different GR configurations. As demonstrated in the red dotted line frame in the figure, different GR configurations will lead to different vibration modes in the corresponding areas in the course of SAWR resonance. The color of the model in the figure represents the magnitude of the displacement at resonance. The dark red color, which represents the maximum displacement, basically only occurs in the SAWR active area, while the displacement in the GR area is blue, which means that the acoustic wave is attenuated after propagating to this area. When comparing the model without GR to the one with floating GR, focusing solely on the displacement in the GR region, the former appears predominantly light blue, while the latter is mostly dark blue. The comparison indicates that the floating GR can effectively confine vibration within the device's active area, minimizing energy leakage into the GR region. This is the key mechanism of improvement of the Q factor of SAWR from the design of GR structure. Similarly, when comparing the models of floating GR and grounded GR, the displacement in the GR region is obviously smaller in the latter. This result suggests that the grounded GR confines energy within the active area with higher efficiency, leading to a greater improvement in the Q factor of the SAWR.

III. MEASUREMENT AND ANALYSIS

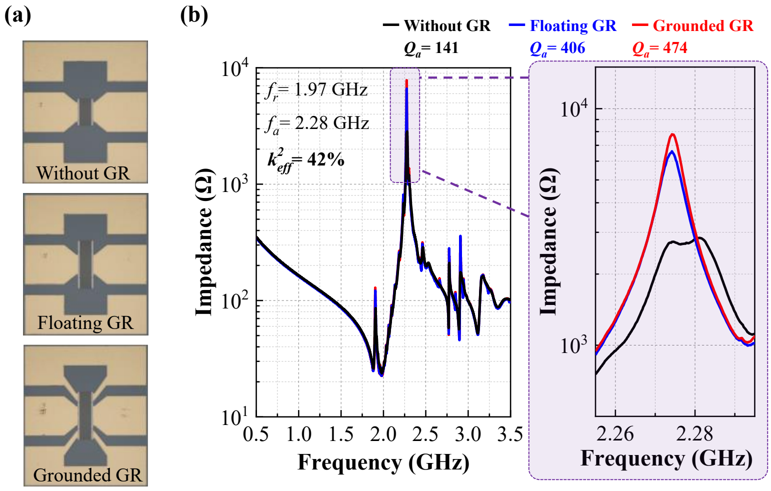

Figure 4. (a) Microscope images of fabricated three kinds of SAWRs: without GR, floating GR and grounded GR. All devices have 50 pairs of IDTs and 0 or 20 pairs of reflectors on each side. (b) Measured frequency responses of these three kinds of SAWRs.

The optimized SAWRs were fabricated using EBL for devices patterning, followed by electrode deposition by E-beam evaporation and standard lift-off processes. The IDTs material and structural parameters were designed based on the optimization discussed in Part II. Additionally, a 5 nm Ti layer was used as an adhesion layer and an 80 nm Au layer was deposited to thicken the probing pads and connection areas. Figures 4(a) and 4(b) show optical microscope images and measured frequency-impedance curves of fabricated SAWRs with three different GR configurations. The f_r of the device is 1.97 GHz while anti-resonance frequency (f_a) is 2.28 GHz. The result suggests that the fabricated SAWR exhibits an ultra-high k^2_{eff} of 42%, where it is extracted by the equation $\pi^2(f_a^2 - f_r^2)/(8f_r^2)$ [21]. The quality factor at the resonance frequency (Q_r) remains relatively low due to the limited conductivity of Pt, which could be further improved by increasing the Au thickness, widening the connections, and applying Au to the busbars. Nevertheless, the trade-off between achieving a higher coupling coefficient and the resulting increase in device resistance must be carefully considered, depending on the specific application. To further illustrate the impact of different GR configurations on improving the Q factor of the SAWR, the quality factor at the anti-resonance frequency (Q_a) are also presented in Figure 4(b), where the Q can be calculated by the equation $f_{r,a}/\Delta f_{r,a-3\text{dB}}$. The Q_a of the SAWR without GR is only 141, while that with the floating GR structure reaches 406, more than twice the former. And the grounded GR design further improves this value to 474, more than three times that of the structure without GR.

Figure 5 presents the frequency distribution and impedance ratio comparison of the main mode and several dominant spurious modes (SMs) within the range of 0.5 to 3.5 GHz. For the SH_0 mode, the grounded GR configuration exhibits the highest impedance ratio, followed by the floating GR, while the GR-free structure shows the lowest. This trend aligns with the variation in Q values discussed earlier. The impedance ratios of SH_0 mode for all three GR configurations exceed 40 dB, whereas most of the SMs remain below 15 dB. Furthermore, the intensity of the SMs, is also influenced by the GR configuration and is notably enhanced by the presence of GRs in the longitudinal array. Among these, the SM at 2.9 GHz is the most significantly amplified, suggesting a higher proportion of longitudinal components in this mode. In contrast, the SM at 3.1 GHz shows minimal enhancement, indicating a smaller longitudinal component contribution.

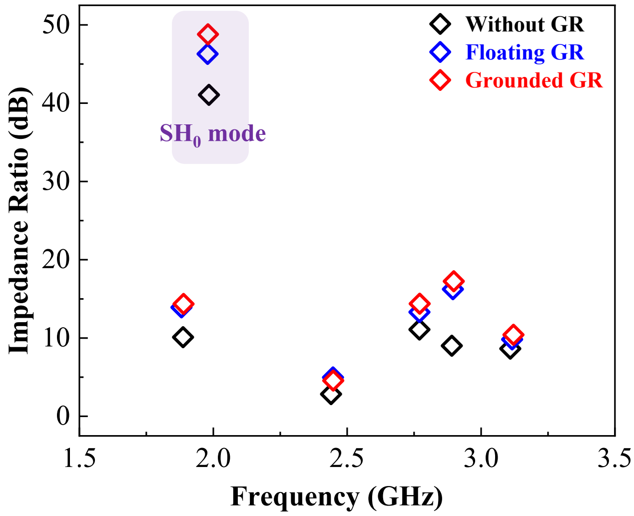

Figure 5. Summary of the frequencies and impedance ratios of the main modes in the range of 0.5 to 3.5 GHz.

To further comprehensively evaluate the effect of the GR structure on the Q factor, the Q values of multiple groups of devices were statistically compared. Figure 6(a) shows the design of dummy IDTs while its width is w_D and the gap between the dummy and real IDTs is w_G.

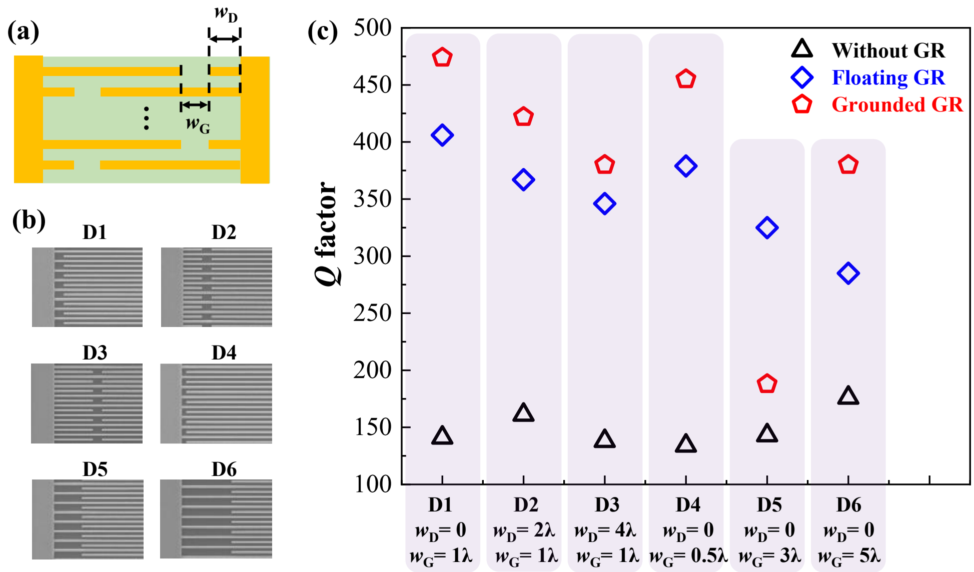

Figure 6. (a) Structural parameters of the width w_D of dummy IDTs and the gap w_G between the dummy and real IDTs. (b) SEM images of fabricated six kinds of SAWRs with different w_D and w_G. (c) Measured Q factors of these six kinds of SAWRs in cases of no GR, floating GR and grounded GR.

Figure 6(b) shows the SEM images of fabricated six kinds of SAWRs with different w_D and w_G while Figure 6(c) shows their Q factors. From the comparison, the effect of the GR structure on the improvement of the Q factor of SAWR can be observed easily, and the grounded GR has a better effect than the floating GR. This result is consistent with results from previous simulations and theoretical analyses. Q values from 18 devices are included in this analysis, 17 of which are consistent with our conclusions. The outlier—device D5 with grounded GR—is attributed to a fabrication defect, as detailed in the supplementary materials. This data point does not reflect the typical behavior of the grounded GR configuration, and its exclusion does not impact the validity of our conclusions.

As mentioned in the introduction part, high-performance SAWRs and FBARs have always been the common goal of academia and industry. Figure 7 summarizes published SAWRs and FBARs where all devices listed here exhibit f_r exceeding 1 GHz. SAWRs and FBARs based on AlN/ScAlN and LN/LT material platforms have excellent performance as mainstream in this field. Therefore, most of the references in Figure 6 are from these two material platforms.

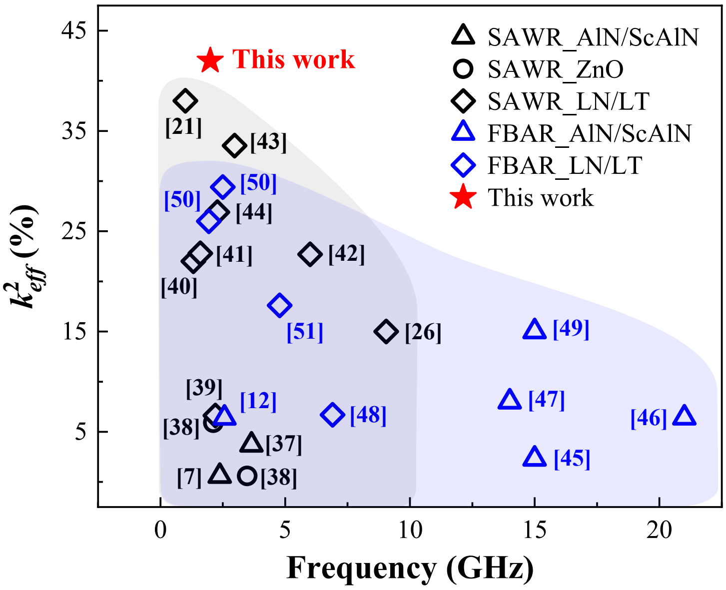

Figure 7. The survey of k^2_{eff} from published SAWRs and FBARs while all f_r are above 1 GHz[7,12,21,26,37-51].

It can be clearly seen that the SAWRs with high k^2_{eff} are all fabricated based on LN/LT films while the highest one can reach 38%. Since the shear piezoelectric coefficients are small, all k^2_{eff} of AlN/ScAlN-SAWRs are very small. However, thanks to the huge improvement of coupling coefficient d_{33} in AlN film due to the high-concentration Sc doping, the k^2_{eff} of FBARs can exceed 15%. Due to intrinsic material properties of LN/LT, the maximum k^2_{eff} of FBAR based on LN/LT is about 30% at most. In this work, the SH-SAWR with 2 GHz f_r and k^2_{eff} of up to 42% is achieved through reasonable and systematic design optimization. To the best of our knowledge, this is the first time that f_r above 1 GHz and k^2_{eff} larger than 40% have been achieved simultaneously among various SAWRs and FBARs.

IV. CONCLUSION

This work proposes a high-performance SH_0 mode SAWR based on the X-cut LNOI platform. FEA simulation and theoretical analysis are systematically investigated for electrode material selection and structural parameters optimization. The results show that Pt electrode and a wavelength of 1.6 μm are the optimal conditions in achieving the maximum k_{eff}^2. Besides, the metallization ratio and electrode thickness are also optimized to obtain the largest k_{eff}^2. The fabricated SAWR exhibits 2 GHz f_r and a 42% ultra-high coupling coefficient is achieved. In addition to optimizing k_{eff}^2, this work also studied the effect of floating and grounded GRs on the Q factor of the device through the combination of simulation and experiment. The experimental results show that the floating GR can increase the Q factor by more than twice, while the grounded GR can increase it by more than three times, which shows good consistency with the simulation and theoretical analyses.

ACKNOWLEDGMENTS

The authors acknowledge the funding support by Singapore National Research Foundation Competitive Research Program (NRF-CRP28-2022-0002) and RIE2025 MTC Individual Research Grant (M22K2c0084).

AUTHOR DECLARATIONS

Conflict of Interest

The authors have no conflicts to disclose.

AUTHOR CONTRIBUTIONS

Tiancheng Luo: Conceptualization (equal); Writing – original draft (equal). **Qibin Zeng:** Data curation (equal); Supervision (equal). **Weifan Cai:** Formal analysis (equal). **Zhi Shiuh Lim:** Writing – review & editing (equal). **Shengwei Zeng:** Data curation (equal). **Samantha Faye Duran Solco:** Validation (equal). **Zhen Ye:** Investigation (equal); Data curation (equal). **Chee Kiang Ivan Tan**: Writing – Review & editing (equal). **Seeram Ramakrishna**: Writing – review & editing (equal); Supervision (equal). **Huajun Liu:** Writing – Review & editing (equal); Supervision (equal).

DATA AVAILABILITY

The data supporting this study's findings are available from the corresponding authors upon request.

REFERENCES

1 K. Yang, C. He, J. Fang *et al.*, "Advanced RF filters for wireless communications," Chip **2**, 100058, (2023).

2 H. Xu, S. Fu, R. Su *et al.*, "SAW Filters on $LiNbO_3$/SiC Heterostructure for 5G n77 and n78 Band Applications," IEEE Trans. Ultrason. Ferroelectr. Freq. Control **70**, 1157-1169, (2023).

3 C. C. W. Ruppel, "Acoustic Wave Filter Technology-A Review," IEEE Trans. Ultrason. Ferroelectr. Freq. Control **64**, 1390-1400, (2017).

4 A. E. Hake, C. Zhao, W. K. Sung *et al.*, "Design and Experimental Assessment of Low-Noise Piezoelectric Microelectromechanical Systems Vibration Sensors," IEEE Sens. J. **21**, 17703-17711, (2021).

5 L. Gao, "K-band lithium niobate microelectromechanical system hybrid filters," Master thesis, University of Illinois at Urbana-Champaign, (2020).

6 I. Kanno, J. Ouyang, J. Akedo *et al.*, "Piezoelectric thin films for MEMS," Appl. Phys. Lett. **122**, 090401, (2023).

7 T. Lu, X. Fang, S. Zhang *et al.*, "High speed surface acoustic wave and laterally excited bulk wave resonator based on single-crystal non-polar AlN film," Appl. Phys. Lett. **123**, 252105, (2023).

8 W. Jiang, J. Chen, X. Liu *et al.*, "Thin film aluminum nitride surface acoustic wave resonators for quantum acoustodynamics," Appl. Phys. Lett. **123**, 024002, (2023).

9 X. Tan, Z. Zhou, L. Zhang *et al.*, "A passive wireless triboelectric sensor via a surface acoustic wave resonator (SAWR)," Nano Energy **78**, 105307, (2020).

10 Y. Guo, M. Kadota & S. Tanaka, "Hetero Acoustic Layer Surface Acoustic Wave Resonator Composed of $LiNbO_3$ and Quartz," IEEE Trans. Ultrason. Ferroelectr. Freq. Control **71**, 182-190, (2024).

11 J. Wang, M. Park, S. Mertin *et al.*, "A Film Bulk Acoustic Resonator Based on Ferroelectric Aluminum Scandium Nitride Films," J. Microelectromechanical Syst. **29**, 741-747, (2020).

12 X. Yi, L. Zhao, P. Ouyang *et al.*, "High-Quality Film Bulk Acoustic Resonators Fabricated on AlN Films Grown by a New Two-Step Method," IEEE Electron Device Lett. **43**, 942-945, (2022).

13 R. Su, J. Shen, Z. Lu *et al.*, "Wideband and Low-Loss Surface Acoustic Wave Filter Based on 150° YX-$LiNbO_3$/SiO_2/Si Structure," IEEE Electron Device Lett. **42**, 438-441, (2021).

14 Y. Liu, Y. Cai, Y. Zhang *et al.*, "Materials, Design, and Characteristics of Bulk Acoustic Wave Resonator: A Review," *Micromachines* **11** (2020).

15 N. Ashraf, Y. Mesbah, A. Emad *et al.*, "Enabling the 5G: Modelling and Design of High Q Film Bulk Acoustic Wave Resonator (FBAR) for High Frequency Applications," in *2020 IEEE International Symposium on Circuits and Systems (ISCAS).* 1-4.

16 E. Butaud, S. Ballandras, M. Bousquet *et al.*, "Innovative Smart Cut™ Piezo On Insulator (POI) Substrates for 5G acoustic filters," in *2020 IEEE International Electron Devices Meeting (IEDM).* 34.36.31-34.36.34.

17 Y. Zhu & Q. Wan, "Lithium niobate/lithium tantalate single-crystal thin films for post-moore era chip applications," Moore and More **1**, 6, (2024).

18 V. Plessky, "XBAR," in *2022 IEEE International Ultrasonics Symposium (IUS).* 1-11.

19 Z. Wen, W. Liu, T. Luo *et al.*, "A laterally excited bulk acoustic resonator with scattering vias in electrodes," Appl. Phys. Lett. **123**, 093501, (2023).

20 J. Koulakis, J. Koskela, W. Yang *et al.*, "XBAR physics and next generation filter design," in *2021 IEEE International Ultrasonics Symposium (IUS).* 1-5.

21 T. H. Hsu, C. H. Tsai, S. S. Tung *et al.*, "Miniature $LiNbO_3$/SiO_2/Si SH-SAW Resonators With Near-Spurious-Free Response," IEEE Electron Device Lett. **44**, 1200-1203, (2023).

22 T. H. Hsu, K. J. Tseng & M. H. Li, "Wideband and High Quality Factor Shear Horizontal SAW Resonators with Improved Temperature Stability in LNOI Platform," in *2021 Joint Conference of the European Frequency and Time Forum and IEEE International Frequency Control Symposium (EFTF/IFCS).* 1-4.

23 A. E. Hassanien, R. Lu & S. Gong, "Near-Zero Drift and High Electromechanical Coupling Acoustic Resonators at > 3.5 GHz," IEEE Trans. Microw. Theory Tech. **69**, 3706-3714, (2021).

24 T. H. Hsu, Z. Q. Lee, C. H. Tsai et al., "Harnessing Acoustic Dispersions in YX-LN/SiO_2/Si SH-SAW Resonators for Electromechanical Coupling Optimization and Rayleigh Mode Suppression," IEEE Trans. Ultrason. Ferroelectr. Freq. Control 70, 1786-1793, (2023).

25 T. H. Hsu, Z. Q. Lee, G. L. Wu et al., "Gold as a Promising Electrode Material for $LiNbO_3$-on-Insulator (LNOI) SH-SAW Resonators: An Experimental Study," IEEE Trans. Ultrason. Ferroelectr. Freq. Control 71, 1324-1334, (2024).

26 T. H. Hsu, J. Campbell, J. Kramer et al. in 2024 IEEE MTT-S International Conference on Microwave Acoustics & Mechanics (IC-MAM). 117-120.

27 T. Suzuki, M. Suzuki & S. Kakio, "Analysis of surface acoustic wave resonance properties on piezoelectric substrates with periodic voids," Jpn. J. Appl. Phys. **62**, SJ1008, (2023).

28 R. Su, S. Fu, J. Shen *et al.*, "Wideband Surface Acoustic Wave Filter at 3.7 GHz With Spurious Mode Mitigation," IEEE Trans. Microw. Theory Tech. **71**, 480-487, (2023).

29 S. Yandrapalli, K. C. S. E, B. Atakan *et al.*, "Fabrication and Analysis of Thin Film Lithum Niobate Resonators for 5GHz Frequency and Large k_t^2 Applications," in *2021 IEEE 34th International Conference on Micro Electro Mechanical Systems (MEMS).* 967-969.

30 M. Kadota, Y. Ishii & S. Tanaka, "Surface Acoustic Wave Resonators With Hetero Acoustic Layer (HAL) Structure Using Lithium Tantalate and Quartz," IEEE Trans. Ultrason. Ferroelectr. Freq. Control **68**, 1955-1964, (2021).

[31] L. Kelly, H. Northfield, S. Rashid *et al.*, "Fabrication of high frequency SAW devices using tri-layer lift-off photolithography," Microelectron. Eng. **253**, 111671, (2022).

[32] S. Wu, Z. Wu, H. Qian *et al.*, "Tilted IDT Designs for Spurious Modes Suppression in $LiNbO_3/SiO_2/Si$ SAW Resonators," IEEE Trans. Electron Devices **70**, 5831-5838, (2023).

[33] J. Wu, S. Zhang, X. Ke *et al.*, "Rotated Interdigital Transducers With Matched Waveguide Boundaries for High-Performance Surface Acoustic Wave Devices," IEEE Trans. Microw. Theory Tech., 1-9, (2024).

[34] P. Zheng, S. Zhang, J. Wu *et al.*, "Near 5-GHz Longitudinal Leaky Surface Acoustic Wave Devices on $LiNbO_3/SiC$ Substrates," IEEE Trans. Microw. Theory Tech. **72**, 1480-1488, (2024).

[35] M. Kwon, I. Ignat, D. Platz *et al.*, "Aluminum nitride surface acoustic wave resonators with high Qf product by optical lithography," Sens. actuators. A Phys. **362**, 114637, (2023).

[36] Y. Liu, B. Lin, Y. Xie *et al.*, "Boosting Performance of SAW Resonator via AlN/ScAlN Composite Films and Dual Reflectors," IEEE Trans. Ultrason. Ferroelectr. Freq. Control **70**, 1239-1245, (2023).

[37] Z. Hao, M. Park, D. G. Kim *et al.*, "Single Crystalline ScAlN Surface Acoustic Wave Resonators with Large Figure of Merit ($Q \times k_t^2$)," in *2019 IEEE MTT-S International Microwave Symposium (IMS).* 786-789.

[38] R. Su, S. Fu, J. Shen *et al.*, "Enhanced Performance of $ZnO/SiO_2/Al2O_3$ Surface Acoustic Wave Devices with Embedded Electrodes," ACS Appl. Mater. Interfaces **12**, 42378-42385, (2020).

[39] J. Wu, S. Zhang, H. Zhou *et al.*, "Low-Loss SAW Devices with $LiTaO_3$ on Extremely High Resistance Substrate," in *2021 IEEE International Ultrasonics Symposium (IUS).* 1-4.

[40] J. Shen, S. Fu, R. Su *et al.*, "High-Performance Surface Acoustic Wave Devices Using $LiNbO_3/SiO_2/SiC$ Multilayered Substrates," IEEE Trans. Microw. Theory Tech. **69**, 3693-3705, (2021).

[41] Y. Yang, L. Gao & S. Gong, "Surface-Acoustic-Wave Devices Based on Lithium Niobate and Amorphous Silicon Thin Films on a Silicon Substrate," IEEE Trans. Microw. Theory Tech. **70**, 5185-5194, (2022).

[42] P. Liu, S. Fu, R. Su *et al.*, "A near spurious-free 6 GHz LLSAW resonator with large electromechanical coupling on X-cut $LiNbO_3/SiC$ bilayer substrate," Appl. Phys. Lett. **122**, 103502, (2023).

[43] S. Huang, Y. Shuai, L. Lv *et al.*, "$LiNbO_3$ Surface Acoustic Wave Resonators with Large Effective Electromechanical Coupling," *Electronics* **12** (2023).

[44] S. Zhang, R. Lu, H. Zhou *et al.*, "Surface Acoustic Wave Devices Using Lithium Niobate on Silicon Carbide," IEEE Trans. Microw. Theory Tech. **68**, 3653-3666, (2020).

[45] W. Zhao, M. J. Asadi, L. Li *et al.*, "15-GHz Epitaxial AlN FBARs on SiC Substrates," IEEE Electron Device Lett. **44**, 903-906, (2023).

[46] S. Cho, O. Barrera, P. Simeoni *et al.*, "55.4 GHz Bulk Acoustic Resonator in Thin-Film Scandium Aluminum Nitride," in *2023 IEEE International Ultrasonics Symposium (IUS).* 1-4.

[47] C. Liu, X. Wang, W. Yang *et al.*, "A $Sc_{0.2}Al_{0.8}N$-based 14 GHz Film Bulk Acoustic Resonator with over 8% Coupling Coefficient and over 400 Quality factor for Ku-band applications," in *2023 IEEE International Ultrasonics Symposium (IUS).* 1-4.

[48] L. C. Sauze, N. Vaxelaire, R. Templier *et al.*, "6.9 GHz Film Bulk Acoustic Resonator based on Pulsed Laser Deposited $LiNbO_3$ Film," in *2023 IEEE International Ultrasonics Symposium (IUS).* 1-4.

[49] X. Wang, C. Liu, Y. Zhang *et al.*, "Thin $Sc_{0.2}Al_{0.8}N$ Film Based 15 GHz Wideband Filter: Towards mmWave Acoustic Filters," in *2023 International Electron Devices Meeting (IEDM).* 1-4.

[50] M. Bousquet, M. Bertucchi, P. Perreau *et al.*, "Single-mode high frequency $LiNbO_3$ Film Bulk Acoustic Resonator," in *2019 IEEE International Ultrasonics Symposium (IUS).* 84-87.

[51] M. Bousquet, P. Perreau, C. Maeder-Pachurka *et al.*, "Lithium niobate film bulk acoustic wave resonator for sub-6 GHz filters," in *2020 IEEE International Ultrasonics Symposium (IUS).* 1-4.